論文 / 著書情報
Article / Book Information

Title	X-ray computed tomography analysis of lithium deposition in all-solid-state lithium-metal batteries with carbon interlayers bonded through various processes
Authors	M. Kodama, N. Uno, Y. Takase, O. Aoki, R. Iwamura, T. Kotaka, K. Aotani, S. Hirai
Citation	Journal of Power Sources Advances, Vol. 26, ,
Pub. date	2024, 2
DOI	https://dx.doi.org/10.1016/j.powera.2024.100142

Journal of Power Sources Advances 26 (2024) 100142

Contents lists available at ScienceDirect

Journal of Power Sources Advances

journal homepage: www.sciencedirect.com/journal/journal-of-power-sources-advances

X-ray computed tomography analysis of lithium deposition in all-solid-state lithium-metal batteries with carbon interlayers bonded through various processes

M. Kodama [a,*], N. Uno [a], Y. Takase [a], O. Aoki [b], R. Iwamura [b], T. Kotaka [b], K. Aotani [b], S. Hirai [a]

[a] Tokyo Institute of Technology, 2-12-1 Ookayama, Meguro-ku, Tokyo, 152-8550, Japan
[b] Nissan Motor Co., Ltd., 1 Natsushima, Yokosuka, Kanagawa, 237-8523, Japan

ARTICLE INFO

Keywords:
All-solid-state lithium-metal battery
Sulfide solid electrolyte
Carbon interlayer
Lithium-metal anode
X-ray computed tomography

ABSTRACT

Lithium-metal anodes are promising electrodes for fabricating high-capacity all-solid-state batteries; however, lithium dendrite growth during charging limits their applicability. One method to suppress lithium dendrite growth is to insert a carbon interlayer between the solid electrolyte and the lithium-metal anode. There are many potential approaches for inserting a carbon interlayer. The optimal conditions for suppressing lithium dendrite growth and ensuring uniform lithium deposition have not yet been established. This study employs X-ray computed tomography to investigate anode-less all-solid-state batteries. Pressurized xenon is used to examine how the carbon interlayer functions and how uniformly lithium is deposited after various carbon interlayer insertion processes. Uniform deposition is observed following simultaneous pressure bonding of the carbon interlayer and compression of the solid electrolyte.

1. Introduction

All-solid-state batteries comprising a lithium-metal anode and a sulfide-based solid electrolyte (SE) are expected to become the next generation of batteries for electric vehicles because of their high energy density, high ionic conductivity, and flame resistance [1]. However, lithium dendrites grow on the anode when such batteries are charged at high current density; they then penetrate the solid electrolyte layer (separator) and cause an internal short circuit, resulting in a loss of battery function [2]. Therefore, to suppress lithium dendrite growth under high-current-density conditions, various strategies that involve adding interfacial layers between the solid electrolyte and lithium-metal anode have been proposed, including insertion of carbon [3], metal [4], or metal oxide [5] interlayers, controlling the shape [6] and mechanical properties [7] of the interface, and introducing three-dimensional nanostructures [8].

Inserting a carbon interlayer between the solid electrolyte and lithium metal is advantageous for practical applications because it is a low-cost technique. The carbon interlayer prevents direct contact between the solid electrolyte and the lithium metal, while suppressing dendrite growth by blocking the electronic conductivity associated with solid electrolyte reduction. Dendrite growth is also suppressed owing to the enhanced electronic conductivity at the interface, which reduces the nonuniformity of the current density and the reaction in general. Because carbon can exist independently of lithium-metal alloying and redox reactions, a carbon interlayer has excellent cycling characteristics and shows low susceptibility to material degradation during charging and discharging [9]. Studies focusing on improving battery performance by introducing a carbon interlayer have demonstrated the potential to achieve high current density. Zheng et al. [10] increased Young's modulus of carbon by creating a hollow carbon structure and performing quenching reactions to minimize changes to the mechanical interface shape by withstanding the stress caused by this shape change. Su et al. [11] mixed carbon particles and polytetrafluoroethylene to prevent direct contact between the solid electrolyte, the lithium metal, and the interfacial byproducts. Lee et al. [12] proposed a mixed layer of carbon and metal particles to promote uniform deposition by increasing the electronic conductivity and reducing the nucleation energy of lithium metal.

Stabilizing lithium deposition by inserting a carbon interlayer has been studied for practical applications in all-solid-state batteries. However, previous studies have only inferred the uniform deposition of lithium metal according to the interfacial shape, which was determined based on electrochemical measurements, e.g., interface resistance and

* Corresponding author.
E-mail address: tanaka.m.ay@m.titech.ac.jp (M. Kodama).

https://doi.org/10.1016/j.powera.2024.100142
Received 25 December 2023; Received in revised form 24 January 2024; Accepted 6 February 2024

critical current density measurements; direct structural measurements have rarely been performed. The sole report describing direct structural measurements involved post-disassembly analyses based on cross-sectional scanning electron microscopy [10]. To our knowledge, nondestructive analysis of the morphology of the lithium-metal anode in an all-solid-state battery with a carbon interlayer has not yet been performed. X-ray computed tomography (CT) can be used to observe the morphological behavior of an all-solid-state battery [13–15]. Some studies have evaluated the structural changes to lithium-metal electrodes following charging and discharging, and the SE-Li interfacial characteristics have been explored. The present study uses X-ray CT to investigate the behavior of a lithium-metal anode in all-solid-state batteries with carbon interlayers. Because the mechanical properties contribute to the deposition of lithium metal, the method used to bond the carbon interlayer to the solid electrolyte also affects the deposition morphology; however, the optimal conditions for inserting a carbon interlayer that promotes uniform deposition of lithium are not yet known.

Based on the research discussed above, this study investigated the lithium deposition structures of all-solid-state batteries with carbon interlayers using X-ray CT. Specifically, we aimed to elucidate the effects of the carbon interlayer bonding method on the lithium deposition morphology. A novel CT contrast method using pressurized xenon was applied because lithium cannot be distinguished from voids using conventional X-ray CT owing to the low X-ray absorption coefficient of lithium metal. The results indicate how the carbon interlayer and the compaction method influence lithium deposition. Mechanistic insights regarding the uniform deposition of lithium without dendrites are expected to contribute to the practical application of lithium-metal anodes in all-solid-state batteries.

2. Experimental procedures

2.1. Material synthesis

The solid electrolyte used in this study, $Li_{5.5}PS_{4.5}Br_{1.5}$ [16], was fabricated using a mechanical milling process. To obtain 3 g of $Li_{5.5}PS_{4.5}Br_{1.5}$, appropriate amounts of Li_2S (99.98%, Sigma-Aldrich), P_2S_5 (99%, Merck), and LiBr (>99%, Wako) were placed into a zirconia pot (50 mL), along with the grinding aid (diethyl ether, 0.2 mL, >99.5%, Hayashi Pure Chemical) and 16 zirconia balls (φ = 10 mm). Mechanical milling was carried out with a high-energy vibration mill (Emax, Retch) at 1200 rpm for 10 h, after which the material was placed into an aluminum crucible and heat-treated at 400 °C for 10 h in an electric furnace (Mini-BS1, Nitto Kagaku) to obtain $Li_{5.5}PS_{4.5}Br_{1.5}$. All of the processes were performed in a low-dew-point (<−80 °Cdp) argon-filled glove box (Miwa Manufacturing). The ionic conductivity of the obtained $Li_{5.5}PS_{4.5}Br_{1.5}$ material compressed at 400 MPa was 4.0 mS/cm at 25 °C. This conductivity is consistent with that reported by Chuang et al. [16].

2.2. Cell assembly

Using $Li_{5.5}PS_{4.5}Br_{1.5}$, an anode-less half-cell was constructed in an X-ray CT imaging jig (Fig. 1). The half-cell ① was constructed inside a cylinder ② (inner diameter = 1 mm) made of polyether ether ketone (PEEK), which is a material with high X-ray transmission [17]. The PEEK cylinder was double-layered, with the outer PEEK cylinder providing gas sealing and the inner PEEK cylinder providing constraints around the outer edge of the cell. The inner PEEK cylinder slid within the outer PEEK cylinder to ensure that the pressure was correctly applied to the half-cell, even when a low stack pressure was induced. A spring ⑤ was attached to the lower stainless-steel rod ④. The entire CT imaging jig was hermetically sealed to prevent the degradation of the sulfide solid electrolyte and lithium metal due to the flow of water vapor, nitrogen, and oxygen from the outside. A molecular sieve (3A, Kanto Chemical) was also enclosed in the cell as a dehumidifier to prevent degradation due to water vapor adsorbed on the jig's inner wall [18]. Bellows valves ⑥ were installed to allow gas replacement inside the jig. The gas inside the jig could be replaced with argon or xenon through these valves at a maximum pressure of 8 atm.

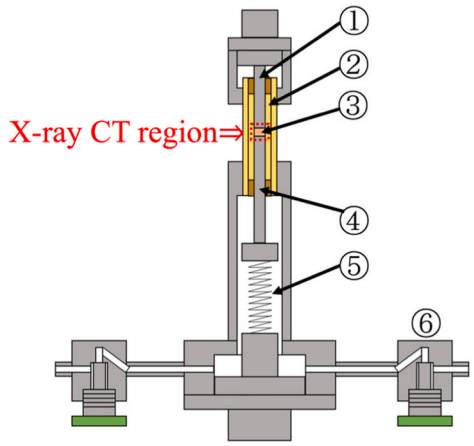

Fig. 1. High-pressure xenon-filled X-ray CT imaging jig. ①: Upper current collector; ②: PEEK tube; ③: anode-less half-cell; ④: lower current collector; ⑤: pressure-control spring; ⑥: gas valve.

2.3. X-ray CT imaging and cell charging

After constructing the half-cell in the CT imaging jig, the jig was placed into the X-ray CT system, and CT imaging was conducted before charging the cell. A laboratory-scale CT system with quasi-parallel optics (customized nano3DX, Rigaku) was used for this CT imaging [19]. A rotating cathode X-ray tube with a molybdenum target served as the X-ray source. The X-rays were generated at an acceleration voltage of 44 kV and an applied current of 66 mA. The generated X-rays were mainly molybdenum Kα rays (17 keV). The CT imaging jig was placed on a rotating stage, which rotated 180° in 0.18° increments, and 1000 X-ray transmission images were captured using an X-ray microscope. The CT images were reconstructed by a computer; the voxel size of the CT images was 540 nm × 540 nm × 540 nm. After initial CT imaging, the jig was connected to a charge–discharge system (Electrofield, EF-7100), and lithium was deposited on the anode. Finally, more CT images were obtained to examine the state of lithium deposition.

3. Results and discussion

To enable X-ray CT imaging of the lithium-metal anode, pressurized xenon was introduced to fill in the entire jig. We then investigated whether the void area and lithium metal could be distinguished in the CT images. The lithium deposition morphology under various pressure-bonding conditions of the carbon interlayer and without a carbon interlayer was then analyzed.

3.1. X-ray CT imaging of lithium metal with xenon

X-ray CT provides three-dimensional images by reconstructing a set of X-ray transmission images taken while rotating the sample [20]. Therefore, the image information captured in the CT image corresponds to the differences in X-ray transmittance, which allow identification of the material in the CT image. The X-ray absorption coefficients of lithium metal, carbon, 1 atm argon, and 6 atm xenon are shown in Fig. 2 (a). To evaluate the lithium deposition in an all-solid-state battery with a carbon interlayer, it was necessary to distinguish the lithium metal from carbon and voids. If a cell is constructed in an argon-filled glove box, the entire cell is filled with argon at 1 atm, and the voids are also filled with

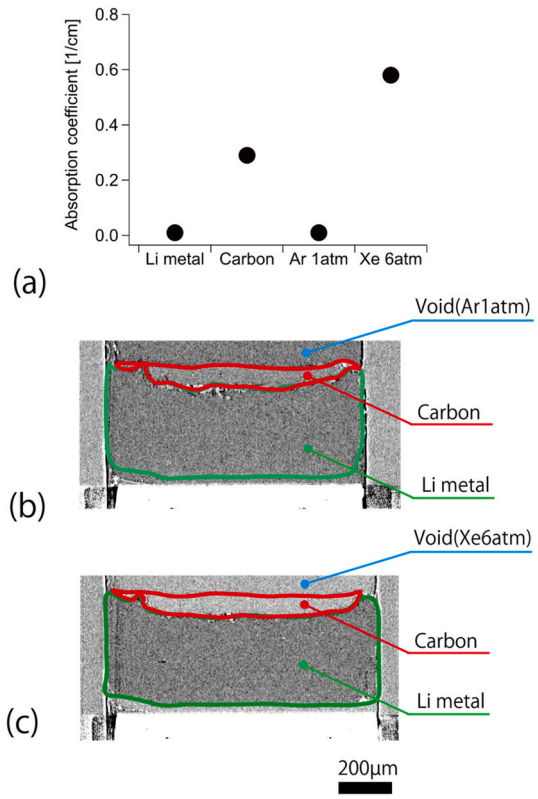

Fig. 2. (a) X-ray absorption coefficient of each material. (b) Cross-sectional CT image of the 1 atm argon-filled cell. (c) Cross-sectional CT image of the 6 atm xenon-filled cell.

argon at 1 atm. In this case, both the lithium metal and the argon have extremely low X-ray absorption coefficients, which makes it difficult to distinguish them in an X-ray CT image. A CT cross-sectional image of a dummy cell fabricated by loading lithium metal and carbon into the CT imaging jig is shown in Fig. 2(b). In this case, the void area contained 1 atm argon, which was the atmosphere in the glove box. It is difficult to distinguish between the lithium metal and voids in this image because the voids and lithium metal have the same brightness. In addition, it is difficult to distinguish the lithium metal from the voids using phase-contrast CT with phase recovery, which our research group has previously reported [21]. In this study, we aimed to discriminate between voids and lithium metal by introducing a gas with low X-ray transmittance into the voids. Xenon at 6 atm has a high X-ray absorption coefficient (Fig. 2(a)). Therefore, the cell was filled with xenon at 6 atm through the valve of the CT imaging jig. Before filling the cell, the argon gas inside the cell was removed by vacuum pumping. A CT cross-sectional image of the dummy cell filled with xenon at 6 atm is shown in Fig. 2(c). In contrast to the cell filled with argon at 1 atm, the image of the cell filled with xenon at 6 atm reveals that the voids and lithium metal could be easily distinguished. This result confirmed that voids can be distinguished from lithium metal in X-ray CT images by introducing high-pressure xenon gas.

3.2. Lithium deposition behavior without a carbon interlayer

First, experiments were performed on an anode-less cell without a carbon interlayer. To construct the cell, the solid electrolyte was pressed at 400 MPa, indium lithium (InLi) was attached, and a stack pressure of 3.0 MPa was applied. A CT cross-sectional image of the anode-less cell without a carbon interlayer before charging is shown in Fig. 3(a). Before charging, only the electrolyte and current collector were observed, and the electrolyte was so tightly packed that no large voids were detected.

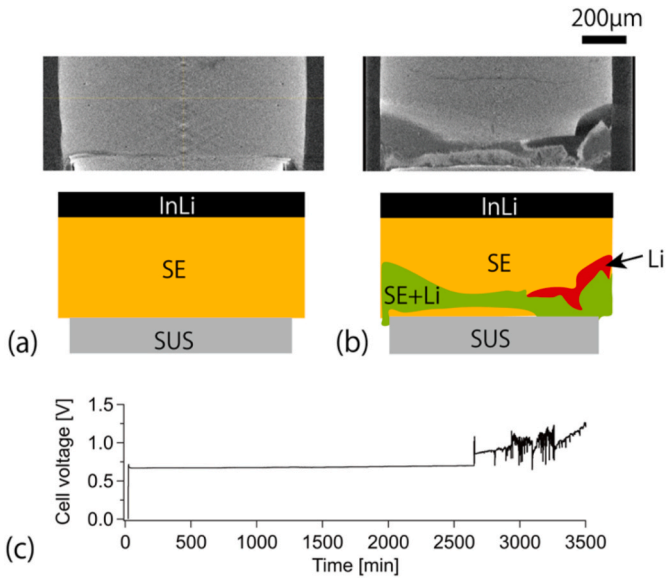

Fig. 3. Cross-sectional X-ray CT images of the anode-less battery without a carbon interlayer (a) before charging and (b) after charging for 3500 min. (c) Cell voltage during charging.

The CT cross-sectional image after charging at 0.2 mA/cm^2 is shown in Fig. 3(b), and the variation in the cell voltage during charging is shown in Fig. 3(c). In an ideal anode-less cell, lithium should be smoothly deposited between the current collector and the electrolyte layer during charging; however, in this case, lithium was deposited into the electrolyte, as shown in Fig. 3(b). This result is consistent with that reported by Otoyama et al. [13]. Two forms of lithium deposition were observed. The first was a region of dark mass in the CT image, where lithium precipitated as a large structure. The second was an area of intermediate brightness in the CT image between the lithium and the solid electrolyte (Fig. 3 (b) "SE + Li"); here, lithium was deposited as a fine structure in the solid electrolyte with low CT resolution, and it is difficult to determine its internal structure. The cell voltage during charging remained stable at approximately 0.622 V for the first 2600 min (Fig. 3(c)). This corresponds to the potential difference between InLi and lithium metal. A steep voltage increase occurred at 2600 min, and the voltage fluctuated thereafter. This voltage increase and fluctuation were considered to be due to the heterogeneity and instability of the reaction associated with dendrite precipitation.

3.3. Lithium deposition behavior with carbon interlayers bonded under various conditions

Charging and CT imaging were then performed with a carbon interlayer inserted in the cell. These experiments were conducted using three cell construction (i.e., carbon interlayer bonding) methods. The construction method used for each cell, the variations in the cell voltage during charging, and the CT cross-sectional images after charging are presented in Fig. 4. The experiments were repeated multiple times under each set of conditions, and considering that similar results were obtained, only representative results for each are presented herein.

In process 1, the carbon interlayer was weakly pressed onto the solid electrolyte. Specifically, the solid electrolyte powder was compressed at 400 MPa, the carbon interlayer was weakly pressure-bonded at 3.0 MPa, and then, InLi was loaded and charged at 0.2 mA/cm^2 under a stack pressure of 3.0 MPa. In process 2, the carbon interlayer was strongly pressed onto the solid electrolyte layer. Specifically, the solid electrolyte powder was compressed at 400 MPa, the carbon interlayer was strongly pressure-bonded at 400 MPa, and then, InLi was loaded and charged at 0.2 mA/cm^2 under a stack pressure of 3.0 MPa. Process 3 involved

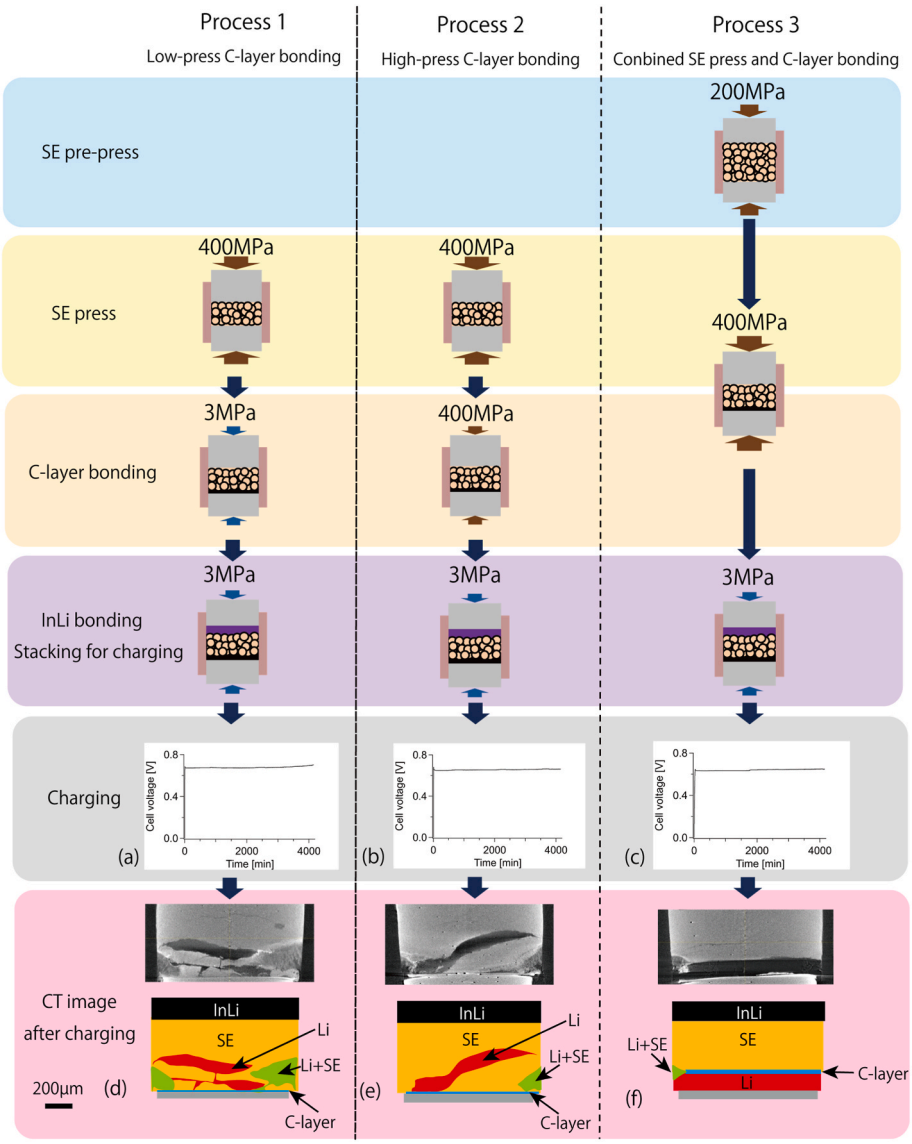

Fig. 4. Cell assembly method. (a–c) Cell voltage during charging for 4000 min. (d–f) Cross-sectional X-ray CT images of the anode-less batteries with carbon interlayers.

simultaneous compression of the solid electrolyte powder and strong pressure bonding of the carbon interlayer. Specifically, the solid electrolyte powder was temporarily compressed at 100 MPa, the carbon interlayer was loaded, the solid electrolyte was fully compressed, and the carbon interlayer was strongly pressure-bonded at 400 MPa; finally, the InLi was loaded and charged at 0.2 mA/cm^2 under a stack pressure of 3.0 MPa.

The variations in the cell voltage during the charging process for the cells containing carbon layers constructed via processes 1–3 are shown in Fig. 4(a–c), respectively. For all three processes, although there was a slight increase in the cell voltage up to 4000 min after the start of charging, the cell voltage almost reached 0.622 V, which is the potential difference between InLi and lithium metal. However, significant differences were observed in the CT cross-sectional images after charging (Fig. 4(d–f)). For processes 1 (Fig. 4(d)) and 2 (Fig. 4(e)), lithium deposition was observed inside the solid electrolyte, similar to the cell with no carbon interlayer. The carbon interlayer existed on the current-collector surface, and therefore, ideal (i.e., uniform) lithium deposition between the carbon interlayer and the current collector could not be confirmed for processes 1 and 2. These results confirmed that the carbon interlayer did not function correctly when it was inserted after compressing the solid electrolyte powder. In contrast, solid electrolyte compression and carbon interlayer pressure bonding were performed simultaneously in process 3 (Fig. 4(f)). In this case, lithium deposition did not occur inside the solid electrolyte, and ideal lithium deposition between the carbon interlayer and current collector was confirmed. Moreover, the estimated thickness of Li deposition, calculated based on the current density and the charging duration, was 65 μm, consistent with the Li deposition thickness in Fig. 4(f).

These results indicate that an ideal carbon interlayer can be formed by simultaneously compressing the solid electrolyte and adhering the carbon interlayer to the solid electrolyte. The carbon interlayer only functioned correctly when it was pressure-bonded simultaneously with (and not after) the shaping of the solid electrolyte because of the work-hardening of the solid electrolyte. When the solid electrolyte was shaped and set first (e.g., in processes 1 and 2), the solid electrolyte plastically deformed during formation, which was believed to induce the work-hardening of the solid electrolyte. A work-hardened solid electrolyte exhibits reduced formability, making it difficult for the carbon interlayer to bond to the solid electrolyte. This results in poor contact between the carbon interlayer and the solid electrolyte, which allows lithium deposition at the interface and fails to suppress dendrite growth. In contrast,

when solid electrolyte shaping and carbon interlayer pressing are performed simultaneously, the carbon interlayer presses against the solid electrolyte before the solid electrolyte hardens, resulting in strong adhesion between the two layers. As a result, lithium deposition on the carbon interlayer and solid electrolyte are suppressed, and lithium deposition occurs between the carbon interlayer and the current collector.

In this study, CT imaging was only conducted after charging to examine the lithium deposition morphology. This method is considered sufficient for determining whether the deposition morphology is uniform; however, it is reasonable to assume that time-lapse CT, which involves stopping the charging midway for imaging, could further elucidate the dynamic behavior during nonuniform deposition. This will be an interesting subject for future research.

4. Conclusions

Lithium-metal solid-state batteries with and without carbon interlayers were investigated by X-ray CT measurements to elucidate the lithium-metal deposition behavior following various carbon interlayer insertion methods. The low X-ray absorption coefficient of lithium metal makes it difficult to distinguish between voids and lithium in normal X-ray CT images. However, this issue was resolved by filling the cell with pressurized xenon, which has a high X-ray absorption coefficient, allowing for clear differentiation between lithium metal and voids. Lithium-metal deposition was inhomogeneous when the carbon interlayer was bonded after compressing the solid electrolyte powder. In contrast, if the solid electrolyte and carbon interlayer were compressed simultaneously, the carbon interlayer effectively suppressed this inhomogeneity, resulting in a more uniform deposition of lithium metal between the carbon interlayer and the current collector.

Based on the results presented herein, simultaneous powder compaction of the solid electrolyte and pressing of the carbon interlayer is an effective strategy for enhancing the performance of anode-less all-solid-state batteries.

CRediT authorship contribution statement

M. Kodama: Writing – original draft, Methodology. **N. Uno:** Resources, Methodology, Investigation. **Y. Takase:** Resources, Methodology, Investigation. **O. Aoki:** Resources, Methodology, Investigation. **R. Iwamura:** Resources. **T. Kotaka:** Supervision, Conceptualization. **K. Aotani:** Supervision, Conceptualization. **S. Hirai:** Project administration.

Declaration of competing interest

The authors declare that they have no known competing financial interests or personal relationships that could have appeared to influence the work reported in this paper.

Data availability

Data will be made available on request.

Acknowledgments

X-ray CT imaging with high-pressure xenon was supported by Prof. Yoshihiro Okuno of the Tokyo Institute of Technology. We also thank Suzanne Adam, PhD, from Edanz (https://jp.edanz.com/ac) for editing a draft of this manuscript.

References

[1] S. Xia, X. Wu, Z. Zhang, Y. Cui, W. Liu, Practical challenges and future perspectives of all-solid-state lithium-metal batteries, Chem 5 (2019) 753–785, https://doi.org/10.1016/j.chempr.2018.11.013.
[2] P.P. Paul, B.-R. Chen, S.A. Langevin, E.J. Dufek, J. Nelson Weker, J.S. Ko, Interfaces in all solid state Li-metal batteries: a review on instabilities, stabilization strategies, and scalability, Energy Storage Mater. 45 (2022) 969–1001, https://doi.org/10.1016/j.ensm.2021.12.021.
[3] L. Chen, J. Zhang, R. Tong, J. Zhang, H. Wang, G. Shao, C. Wang, Excellent Li/garnet interface wettability achieved by porous hard carbon layer for solid state Li metal battery, Small 18 (2022) 2106142, https://doi.org/10.1002/smll.202106142.
[4] J. Wakasugi, H. Munakata, K. Kanamura, Effect of gold layer on interface resistance between lithium metal anode and Li 6.25 Al 0.25 La 3 Zr 2 O 12 solid electrolyte, J. Electrochem. Soc. 164 (2017) A1022–A1025, https://doi.org/10.1149/2.0471706jes.
[5] X. Han, Y. Gong, K. Fu, X. He, G.T. Hitz, J. Dai, A. Pearse, B. Liu, H. Wang, G. Rubloff, Y. Mo, V. Thangadurai, E.D. Wachsman, L. Hu, Negating interfacial impedance in garnet-based solid-state Li metal batteries, Nat. Mater. 16 (2017) 572–579, https://doi.org/10.1038/nmat4821.
[6] R. Xu, F. Liu, Y. Ye, H. Chen, R.R. Yang, Y. Ma, W. Huang, J. Wan, Y. Cui, A morphologically stable Li/electrolyte interface for all-solid-state batteries enabled by 3D-micropatterned garnet, Adv. Mater. 33 (2021) 2104009, https://doi.org/10.1002/adma.202104009.
[7] M. Kodama, K. Takashima, S. Hirai, Improvement of lithium-metal electrode performance of all-solid-state batteries by shot peening on solid-electrolyte surface, J. Power Sources 537 (2022) 231556, https://doi.org/10.1016/j.jpowsour.2022.231556.
[8] C. Wang, Y. Gong, B. Liu, K. Fu, Y. Yao, E. Hitz, Y. Li, J. Dai, S. Xu, W. Luo, E. D. Wachsman, L. Hu, Conformal, Nanoscale ZnO surface modification of garnet-based solid-state electrolyte for lithium metal anodes, Nano Lett. 17 (2017) 565–571, https://doi.org/10.1021/acs.nanolett.6b04695.
[9] H. Xie, C. Yang, Y. Ren, S. Xu, T.R. Hamann, D.W. McOwen, E.D. Wachsman, L. Hu, Amorphous-carbon-coated 3D solid electrolyte for an electro-chemomechanically stable lithium metal anode in solid-state batteries, Nano Lett. 21 (2021) 6163–6170, https://doi.org/10.1021/acs.nanolett.1c01748.
[10] G. Zheng, S.W. Lee, Z. Liang, H.-W. Lee, K. Yan, H. Yao, H. Wang, W. Li, S. Chu, Y. Cui, Interconnected hollow carbon nanospheres for stable lithium metal anodes, Nat. Nanotechnol. 9 (2014) 618–623, https://doi.org/10.1038/nnano.2014.152.
[11] Y. Su, L. Ye, W. Fitzhugh, Y. Wang, E. Gil-González, I. Kim, X. Li, A more stable lithium anode by mechanical constriction for solid state batteries, Energy Environ. Sci. 13 (2020) 908–916, https://doi.org/10.1039/C9EE04007B.
[12] Y.G. Lee, S. Fujiki, C. Jung, N. Suzuki, N. Yashiro, R. Omoda, D.S. Ko, T. Shiratsuchi, T. Sugimoto, S. Ryu, J.H. Ku, T. Watanabe, Y. Park, Y. Aihara, D. Im, Han, IT, High-energy long-cycling all-solid-state lithium metal batteries enabled by silver–carbon composite anodes, Nat. Energy 5 (2020) 299–308, https://doi.org/10.1038/s41560-020-0575-z.
[13] M. Otoyama, M. Suyama, C. Hotehama, H. Kowada, Y. Takeda, K. Ito, A. Sakuda, M. Tatsumisago, A. Hayashi, Visualization and control of chemically induced crack formation in all-solid-state lithium-metal batteries with sulfide electrolyte, ACS Appl. Mater. Interfaces 13 (2021) 5000–5007, https://doi.org/10.1021/acsami.0c18314.
[14] Y. Zheng, S. Zhang, J. Ma, F. Sun, M. Osenberg, A. Hilger, H. Markötter, F. Wilde, I. Manke, Z. Hu, G. Cui, Codependent failure mechanisms between cathode and anode in solid state lithium metal batteries: mediated by uneven ion flux, Sci. Bull. 68 (2023) 813–825, https://doi.org/10.1016/j.scib.2023.03.021.
[15] F. Sun, C. Wang, M. Osenberg, K. Dong, S. Zhang, C. Yang, Y. Wang, A. Hilger, J. Zhang, S. Dong, H. Markötter, I. Manke, G. Cui, Clarifying the electro-chemo-mechanical coupling in Li 10 SnP 2 S 12 based all-solid-state batteries, Adv. Energy Mater. 12 (2022) 2103714, https://doi.org/10.1002/aenm.202103714.
[16] C. Yu, Y. Li, W. Li, K.R. Adair, F. Zhao, M. Willans, J. Liang, Y. Zhao, C. Wang, S. Deng, R. Li, H. Huang, S. Lu, T.-K. Sham, Y. Huang, X. Sun, Enabling ultrafast ionic conductivity in Br-based lithium argyrodite electrolytes for solid-state batteries with different anodes, Energy Storage Mater. 30 (2020) 238–249, https://doi.org/10.1016/j.ensm.2020.04.014.
[17] C. Tan, S. Daemi, O. Taiwo, T. Heenan, D. Brett, P. Shearing, Evolution of electrochemical cell designs for in-situ and operando 3D characterization, Materials 11 (2018) 2157, https://doi.org/10.3390/ma11112157.
[18] M. Kodama, A. Ohashi, H. Adachi, T. Miyuki, A. Takeuchi, M. Yasutake, K. Uesugi, T. Kaburagi, S. Hirai, Three-dimensional structural measurement and material identification of an all-solid-state lithium-ion battery by X-Ray nanotomography and deep learning, J. Power Sourc. Adv. 8 (2021) 100048, https://doi.org/10.1016/j.powera.2021.100048.
[19] M. Kodama, S. Komiyama, A. Ohashi, N. Horikawa, K. Kawamura, S. Hirai, High-pressure in situ X-ray computed tomography and numerical simulation of sulfide solid electrolyte, J. Power Sources 462 (2020) 228160, https://doi.org/10.1016/j.jpowsour.2020.228160.
[20] W.A. Kalender, X-ray computed tomography, Phys. Med. Biol. 51 (2006) R29–R43, https://doi.org/10.1088/0031-9155/51/13/R03.
[21] K. Ohta, T. Wakamatsu, M. Kodama, K. Kawamura, S. Hirai, Laboratory-based x-ray computed tomography for 3D imaging of samples in a diamond anvil cell in situ at high pressures, Rev. Sci. Instrum. 91 (2020) 093703, https://doi.org/10.1063/5.0014486.